Geodetic Investigation of the 2018 Mw 6.4 Hualien Earthquake in Taiwan

James Chen

11/21/2018

Advisor: Mong-Han Huang

GEOL 394

Abstract: A Mw 6.4 Hualien earthquake occurred on Feb 6th 2018, illuminating the local geologic features in the Hualien area. In the coseismic analysis, a three-fault system is required to explain both seismic and geodetic data. This system is composed of a EW striking south dipping fault in the north where the slip initiated. The slip then transferred to a 37 km long west dipping fault located from east of the Milun tableland to west of the north Coastal Range, and finally to a ~8 km long east dipping Milun fault at shallower depth splitting the Milun tableland. In this study, a four month long postseismic surface displacement of the 2018 Hualien earthquake is measured using synthetic aperture radar interferometry (InSAR) and GPS time series. Postseismic displacement during the first four months indicates a cumulative 3-6 cm displacement in the central part of the Milun fault. The four month postseismic time series analysis shows that the area in the north Milun tableland is slowly uplifting, whereas the southeast part of the tableland is subsiding indicating the presence of a curved fault scarp in agreement with the fault trace suggested previously. However, there is minute surface displacement above the main west dipping fault plane west of the north Coastal Range. The lack of postseismic displacement near the north Coastal Range indicates small or deeper afterslip that cannot be detected by InSAR, and the rapid postseismic displacement along the Milun fault implies afterslip along the fault at shallow depth. Using both geodetic techniques and GPS time series, the fault geometry in Hualien can be constrained and our result may clarify fault triggering relationships in future earthquake studies.

1. Introduction

On February 6th, 2018 a moment magnitude 6.4 earthquake was recorded on the north eastern coast of Taiwan in the Hualien district. Major earthquakes frequently occur in this district varying from every four to seven years in between each catastrophic event. This was a deadly earthquake causing severe property damage and loss of life. The quake claimed 17 lives and upwards of 285 people were injured. The earthquake itself is not anomalous since Taiwan is a seismically active region lying along the Ring of Fire in the Pacific Ocean where the Philippine Sea Plate is subducting beneath the Eurasian Plate. The collision rate of these tectonic plates plates is ~82 mm/yr [Lin et. al. 2010].

Shyu identified two faults noted in his 2016 paper which suggests the presence of a south-dipping fault plane extending out from the Liwu Delta north of the Milun tableland. This structure is observed by a cluster of shocks beneath the Coastal Range. The second, much larger fault, is an east-dipping fault plane that is postulated to be a northern extension of the Longitudinal Valley Fault (LVF) system. Seismic analysis suggests that there is another fault plane having the same strike and surface expression dipping west [Huang & Huang 2018]. However, the best-fitting model from the joint inversion suggests that there is only fault slip on the west dipping structure.

This investigation heavily relies upon seismic, GPS, and InSAR analysis. The seismic record has evolved from field survey to seismic stations and satellite imaging over the past several decades. With the aid of high-rate GPS measurements, broadband seismic stations, and Sentinel-1A swath, this investigation can rigorously determine how the main thrust and back thrust faults have formed in the Eurasian/Philippine Sea plate boundary.

The more recent technique making use of the quickly growing network of satellites is called InSAR. InSAR (Synthetic Aperture Radar Interferometry) was first used in topographical studies of the Moon [Zisk et al. 1972]. InSAR, further developing in the 1990s, has matured into an effective tool to detect surface deformities following major seismic events. InSAR is one of

the primary tools used to constrain the fault slip motion in Hualien, Taiwan in Huang & Huang's best-fitting model of the Hualien fault structure.

1.1 Geologic Setting

Taiwan features a series of thrust faults resulting from the subduction of the Philippine Sea Plate beneath the Eurasian plate. The LVF is one of these thrust faults dividing the sedimentary Coastal Range from the Eastern Central Range of Taiwan along the eastern half of the island.

Along the eastern coast of Taiwan, the Luzon Arc in the Philippine Sea Plate is obliquely colliding into the Eurasian continental boundary. Several years ago, Ching et al. (2011) used GPS velocity estimates to illustrate plate corner rotation in the northeastern region of Taiwan. The surface motion velocity vectors largely indicate a westward trend in motion due to the collision of the Philippine Sea plate into the Eurasian plate. However, at the northern tip of the

LVF, the surface velocity vectors flip from sinistral block rotation in the southern half of Taiwan to dextral rotation in the northeastern region of Taiwan (Figure 1). Hualien is a primary region of interest because it lies right where the surface velocity flips from sinistral to dextral rotation. This phenomena is called tectonic escape. The observable increase in the magnitude of the black colored velocity vectors in Figure 1 is a result of the upper crust being pushed westward by the Philippine Sea Plate.

After an earthquake, Coulomb stress begins to accumulate leading up to the next coseismic rupture event. However, were an outside factor introduced to a dynamical system such as a neighboring seismic event, the interseismic strain rates will be enhanced due to the elastic bending of plates. This is demonstrated in earthquake research conducted in South America. Melnick et al. (2017) recently published a paper proposing that the viscous rheology in Chile alone could not have caused the neighboring fault slip, but the sudden increase in elastic strain caused by the 2010 M_w 8.8 Maule earthquake may have boosted the super interseismic phase in the neighboring Illapel region leading to the 2015 M 8.3 Chilean earthquakes. These two events occurred on a large fault system, the Andean megathrust between the Nazca and South

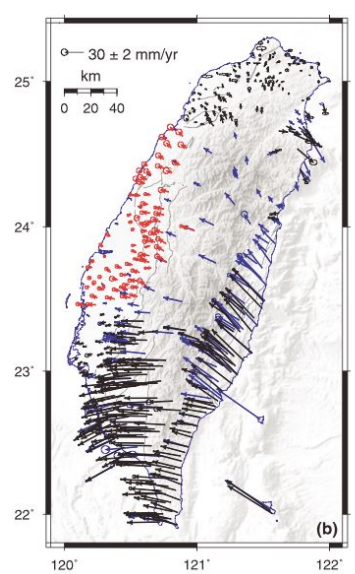


Figure 1. Image is taken from Ching et al. [2011]. Black vectors are derived from the data of Ministry of Interior from 1995 to 2005. Blue vectors are from Hsu et al. [2009].

American Plate. Similarly, the LVF is a thrust fault lying upon a major tectonic plate boundary. The question arises whether an earthquake in the northern fault segment such as the 2018 $\rm M_{\rm w}$ 6.4 Hualien earthquake can influence the triggering of a fault slip in a neighboring region of the LVF system the same way the 2010 earthquake expedited the occurrence of the 2015 Chilean earthquakes.

Successive earthquakes in Taiwan have been observed before, particularly the sequence of the 1951 East Rift Valley earthquakes. Chung et al. (2008) revisited data sets from 1917-1978 to unravel the dynamics of the major plate boundary fault system where the 1951 earthquakes occurred. Their models of the fault system estimate that fault slip may generate seismic events up to $M_{\rm w}$ 7.6 but since only a few earthquakes have come close to this scale of a rupture, they estimate that 24 to 50 percent is a result of aseismic creep.

2. Objectives of research and broader implications

The northern portion of the pacific Luzon Arc is colliding into the Eurasian Plate at a rate of about 82 mm/yr [Hsu et al. 2009]. The colliding point is estimated to be between Suao and Hualien (Figure 2), but little about the subsurface fault structure there is known. It is unclear which fault is directly responsible for the 2018 $\rm M_{\rm w}$ 6.4 Hualien earthquake. Possible candidates for primary fault slip include the Milun Fault, contended as a branch of the LVF [Hsu et al. 1962] and the underlying LV Fault.

Understanding the fault geometry under the Hualien district may inform others about the mechanism responsible for the plate corner rotation at the tip of the Luzon Arc. However, it is difficult to understand the fault system structure at the Longitudinal Valley Fault because there are multiple continental plates converging on the east coast of Taiwan at the LVF. InSAR is an effective technique to acquire crustal deformation over land, but information beneath the ocean is limited because electromagnetic radiation cannot reflect beneath the surface of the water and reveal information about the submerged crust.

There is a shallower unidentified backthrust fault above the primary west dipping fault. InSAR is used to constrain the fault structure in the Hualien district and a postseismic slip analysis to characterize the viscous rheology in the northern tip of the LVF following the 2018 $M_{\rm w}$ 6.4 Hualien earthquake. Shallow afterslip is expected to occur north and south of the coseismic rupture in the first month of the postseismic phase.

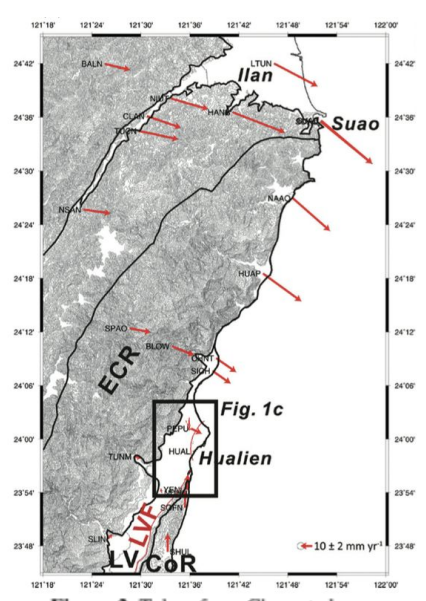


Figure 2. Taken from Chen et al. 2008. Close up regional map of Suao and Hualien, Taiwan.

3. Experimental Design

The CWB of Taiwan released a catalog of the foreshocks starting from February 4th until February 28th 2018. This time frame spans from the pre-shock period through the early post-seismic phase of the earthquake cycle in Hualien. A histogram of the depth reveals that the majority of shocks lie within a depth of 6-12 km.

In the aftershock vs coulomb stress change plot, the expected model follows this step function:

$$f(x) = \begin{cases} 0 & , x < 0 \\ x & , x > 0 \end{cases}$$

The investigation of the subsurface architecture of Hualien combine coseismic and afterslip modeling. Coseismic results will be obtained from interferometry. The coseismic slip inversion is be based on the method used in Hartzell and Heaton (1983) as implemented in Huang et al. (2013). An overall time series is created from 2014 to March 2018.

This investigation uses Coulomb 3.3 to extract stress changes from the latest solution of the fault geometry. Coulomb 3.3 is a program which calculates static stress, strain, and stresses caused by fault slip. Coulomb does not account for dynamic stresses, pore-fluid diffusion, and viscoelastic rebound. In addition, Coulomb uses an elastic half space model in contrast to a layered-cake earth model with varying elastic stiffness. This means that if the difference in the layered modeling or effects of the other physical processes significantly impacts the likelihood of a earthquake happening, the model used by Coulomb will not pick up these physical contributing factors.

A goal of this study is to understand the behavior of how Coulomb stress is distributed during the earthquake cycle. The earthquake cycle begins with the locking of tectonic plates during the interseismic phase, where kinetic energy is increasingly being stored in the crust. The phase when the fault slips and the potential energy is released is called coseismic rupture. Following the primary event as the stress from the shock ripples through the earth and transfers energy into the surrounding rheology

Geodetic and seismological observations is processed in Coulomb

coseismic

Figure 3. Unwrapped interferogram of the coscismic rupture occurring on Feb 6th, 2018 in Hualien. Color scale resized from blue to red indicating maximum subsidence and maximum uplift respectively.

3.3 is used to capture how the stress within the crust evolves on the spatiotemporal scale. The stress change distribution calculated from Coulomb 3.3 is overlays the location of aftershocks. The aftershock data is provided from CWB's catalog of aftershocks for the 2018 Hualien Earthquake. The coefficient of friction is assumed to be 0.3 in standard with the majority of lithospheric models and the Young's modulus is assumed to be 8E5 Pa.

3.1 InSAR Calibration

In the past, SAR used methods such as 3 or 4 pass across-track interferometry for the purpose of calibrating the topography and distinguish surface displacement from the regional topography. With the launch of the SRTM (Shuttle Radar Topography Mission) in 2000, this method is no longer necessary because this mission provides a precise global Digital Elevation Model (DEM). In this investigation, we source our DEM from the Vertex database hosted by the Alaska Satellite Facility. The topsApp.py script removes the topographic phase for us using this DEM as reference.

Intrinsically, InSAR phase error or standard deviation is directly proportional to the perpendicular baseline length. The baseline is the physical distance between the origin of the first and second look position of the orbiting satellite. The greater the baseline length, the smaller the standard deviation in vertical displacement. However when the baseline length is too small, the fringes which appear on the interferogram will be indistinguishable. Currently the Sentinel 1A satellite used in this investigation uses C-band microwave radiation corresponding to a displacement of 28 mm for a single period in phase. This is optimal for detecting centimeter scale displacement commonly caused in coseismic rupture.

Uncertainties in the vertical displacement measurements can be calculated with this formulation:

$$\sigma_z = -\frac{\lambda}{4\pi} \frac{r \sin \vartheta}{b_{\perp}} \sigma_{\varphi} \tag{1}$$

The standard deviation in InSAR height measurements σ_z is inversely proportional to the perpendicular baseline b_\perp , ϑ is the side-looking angle of the satellite, and r is the line of sight (LOS) distance between the satellite and the point of reflection on the surface of the earth [Pepe and Calo 2017].

Other sources of error include statistical errors and metrology errors, and data gaps. Statistical errors may be factored in by Nyquist or quantization noise when collecting signals through the satellite receiver [Burgmann et al. 2000]. Varying atmospheric conditions are also introduced as metrology errors because electromagnetic waves travel differently in humid and dry conditions. Also, data gaps may appear in the complex product because the physical look angle of the satellite is not great enough to receive signals from behind slopes, particularly in mountain belts where there are steep slopes.

6. Results

Aftershock histogram shows that the majority of shocks occur 8 km below the surface since it is where the peak of the gaussian distribution is located.

The seismic aftershock data at depths 6,8, and 10 km the fits the model except for the 12 km depth cross section. Also, the tapering of the edges at +6 bars at each cross section can be taken into account by the increasing rarity of large quantities of coulomb stress change.

0.A Supplementary Figures

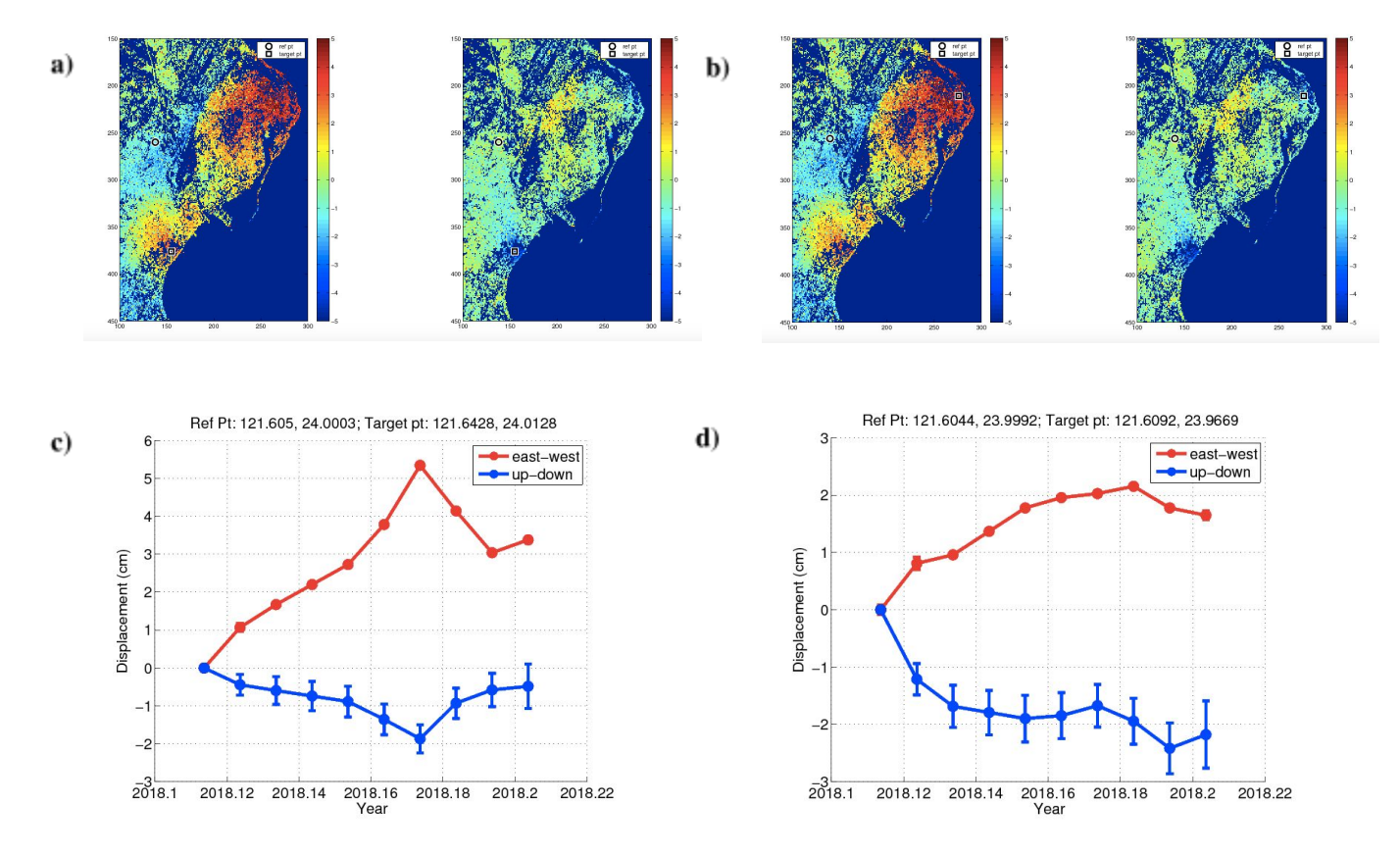


Figure 4. The same postseismic pair product is chosen for both (a) and (b). The left box contains East-West displacement and the right box contains Up-Down displacement. (a) contains the northern target point and (b) contains the southern target point. (c) and (d) are the postseismic time series for (a) and (b) respectively

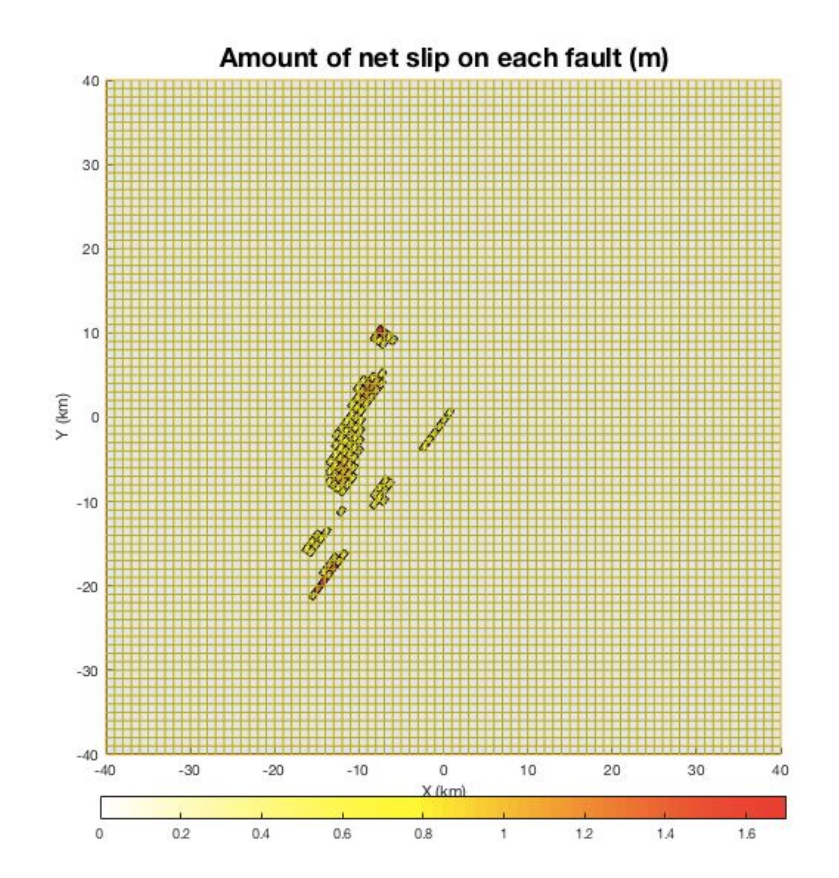
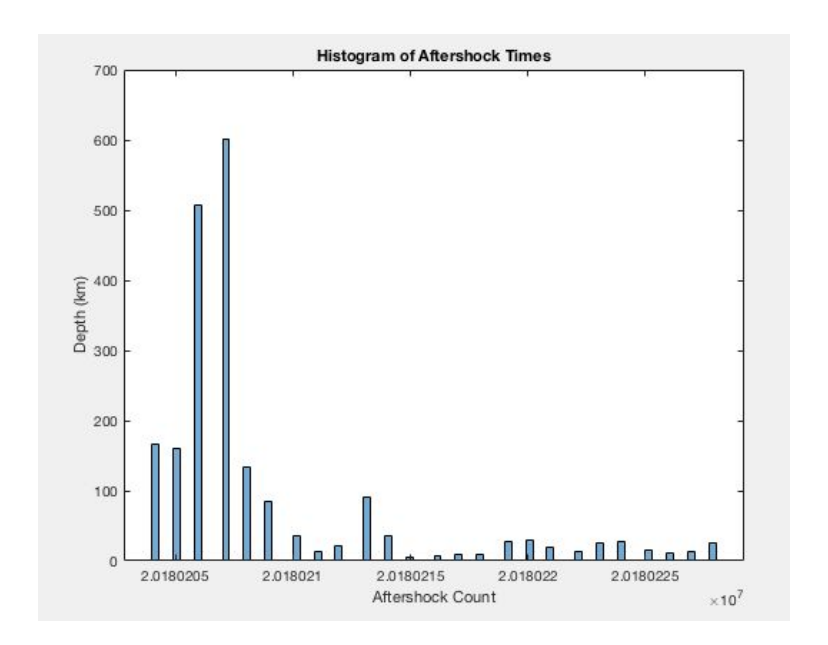


Figure 5. Overhead view of receiver fault. Top right corner of receiver fault is used as the center of the coordinate axes



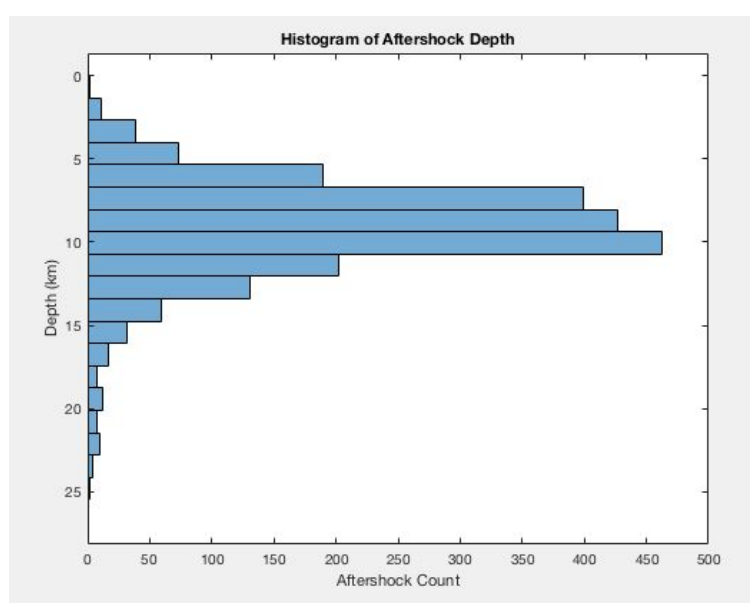
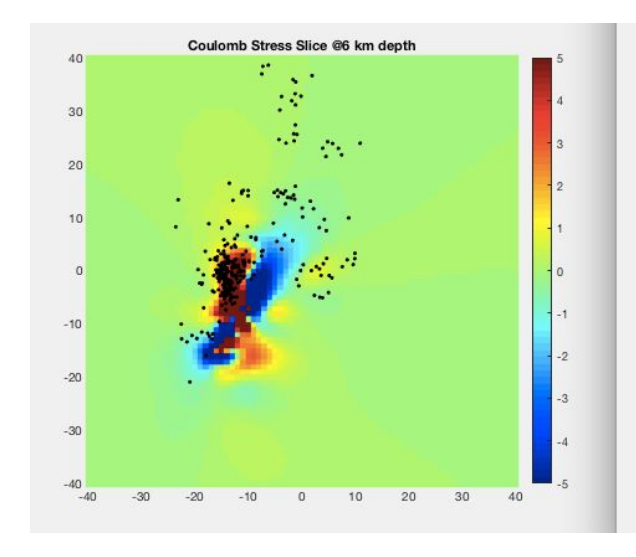
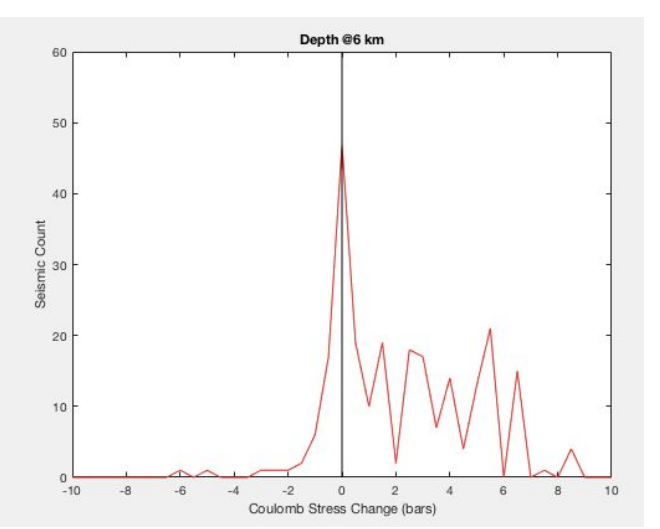
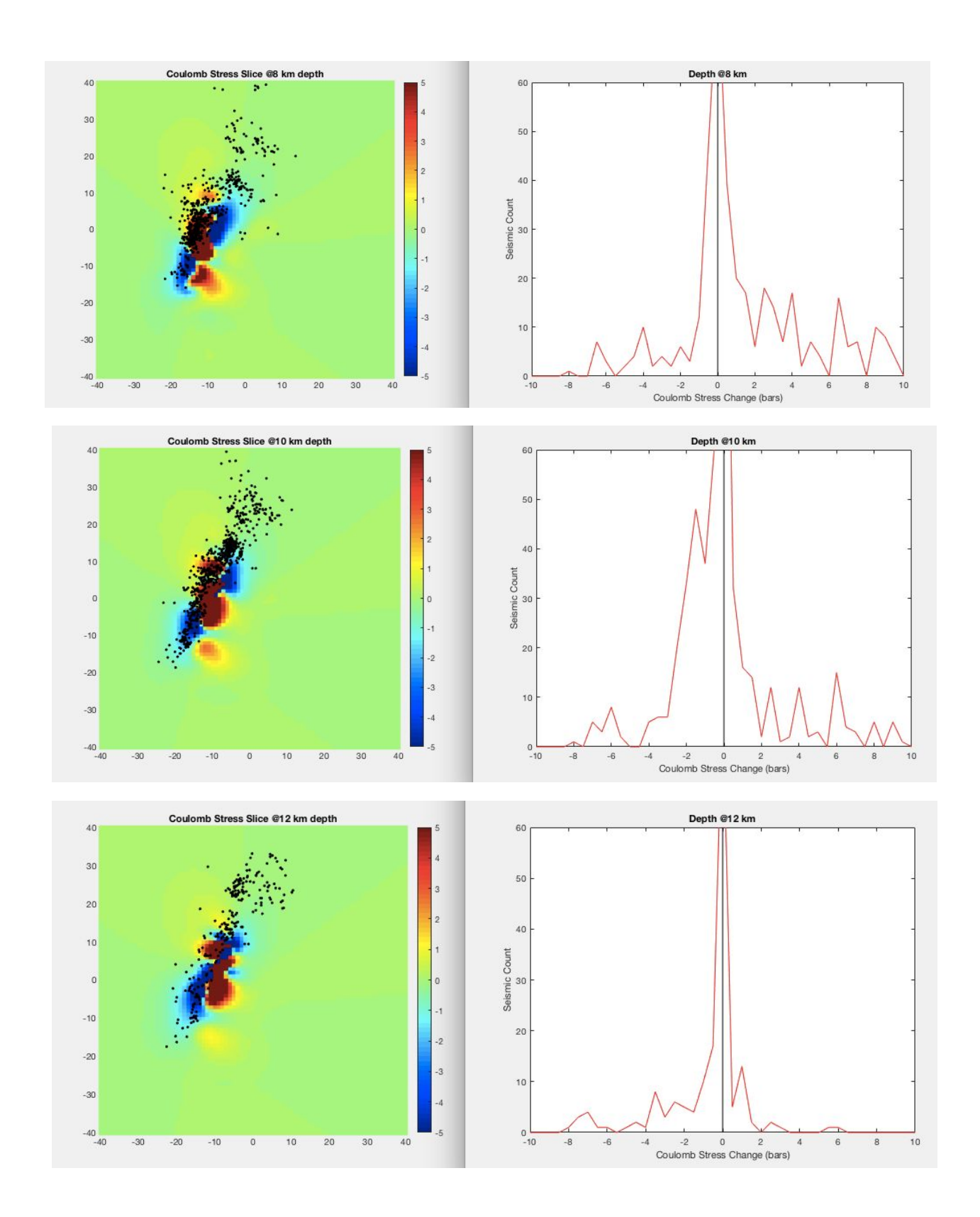


Figure 6. Left. Histogram of the frequency of aftershocks recorded beginning on Feb. 4th, and ending on Feb. 28th, 2018. Right. Histogram of frequency of aftershocks depending upon depth from the surface







0.B Bibliography

- Bürgmann, R., P.-A. Rosen, E.-J. Fielding (2000), Synthetic Aperture Radar Interferometry to Measure Earth's Surface Topography and Its Deformation, *Annual Review of Earth and Planetary Sciences*, 28. 169-209, 10.1146/annurev.earth.28.1.169.
- Ching, K.-E., R.-J. Rau, K. M. Johnson, J.-C. Lee, and J.-C. Hu (2011), Present-day kinematics of active mountain building in Taiwan from GPS observations during 1995–2005, *J. Geophys. Res.*, 116, B09405, doi:10.1029/2010JB008058.
- Chung, L.-H., Y.-G. Chen, Y.-M. Wu, J.-B.-H. Shyu, Y.-T. Kuo, Y.-N.-N. Lin (2008), Seismogenic faults along the major suture of the plate boundary deduced by dislocation modeling of coseismic displacements of the 1951 M7.3 Hualien—Taitung earthquake sequence in eastern Taiwan, *Earth and Planetary Science Letters*, 269(3–4), 416-426, ISSN 0012-821X, doi:10.1016/j.epsl.2008.02.035.
- Hartzell, S. H., T. H. Heaton (1983); Inversion of strong ground motion and teleseismic waveform data for the fault rupture history of the 1979 Imperial Valley, California, earthquake. *Bulletin of the Seismological Society of America*; 73 (6A): 1553–1583.
- Huang, M.-H., D. Dreger, R. Burgmann, S.-H. Yoo, and M. Hashimoto (2013). Joint inversion of seismic and geodetic data for the source of the 2010 March 4, Mw 6.3 Jia-Shian, SW Taiwan, earthquake, *Geophys. J. Int.* 193, 1608–1626, doi: 10.1093/gji/ggt058.
- Huang, M.-H., H.-H. Huang (2018); The Complexity of the 2018 Mw 6.4 Hualien Earthquake in East Taiwan, *Geophys. Res. Lett.* (In review).
- Huang, M.-H., H. Tung, E. J. Fielding, H.-H. Huang, C. Liang, C. Huang, and J.-C. Hu (2016), Multiple fault slip triggered above the 2016 Mw 6.4 MeiNong earthquake in Taiwan, *Geophys. Res. Lett.*, 43, 7459–7467, doi:10.1002/2016GL069351.
- Hsu, T. L. (1962), Recent faulting in the Longitudinal Valley of eastern Taiwan, *Mem. Geol. Soc. China*, 1, 95–102.
- Hsu, Y.-J., S.-B. Yu, M. Simons, L.-C. Kuo, and H.-Y. Chen (2009), Interseismic crustal deformation in the Taiwan plate boundary zone revealed by GPS observations, seismicity, and earthquake focal mechanisms, *Tectonophysics*, 479, 4–18, doi:10.1016/j.tecto.2008.11.016.
- Lin, K.-C., J.-C. Hu, K.-E. Ching, J. Angelier, R.-J. Rau, S.-B. Yu, C.-H Tsai, T.-C. Shin, and M.-H. Huang (2010), GPS Crustal Deformation, Strain Rate, and Seismic Activity after the 1999 Chi-Chi Earthquake in Taiwan, *J. Geophys. Res.*, 115, B07404, doi:10.1029/2009JB006417.
- Melnick, D., M. Moreno, J. Quinteros, J. C. Baez, Z. Deng, S. Li, and O. Oncken (2017), The super-interseismic phase of the megathrust earthquake cycle in Chile, Geophys. Res. Lett., 44, 784–791, doi:10.1002/2016GL071845.
- Pepe, A., F. Caló (2017), A Review of Interferometric Synthetic Aperture RADAR (InSAR) Multi-Track Approaches for the Retrieval of Earth's Surface Displacements, *Appl. Sci.*, 7, 1264, doi:10.3390/app7121264.
- Zisk S.-H. (1972), Lunar topography: first radar-interferometer measurements of the Alphonsus-Ptolemaeus- Arzachel region, *Science*, 178, 977–980.